Model-free control of a magnetically supported plate

P.M. Scherer [a,*], A. Othmane [b], J. Rudolph [a]

[a] *Chair of Systems Theory and Control Engineering, Saarland University, Campus A5 1, Saarbruecken, 66123, Germany*
[b] *Systems Modeling and Simulation, Saarland University, Campus A5 1, Saarbruecken, 66123, Germany*

ARTICLE INFO

ABSTRACT

Established model-based methods often use a combination of state feedback and observer to control complex systems. They rely on detailed mathematical models that are often hard to derive. Nonetheless, such methods may achieve a high level of accuracy, which justifies the cumbersome modelling. An alternative approach is model-free control, in a form introduced by Fliess and Join, where the system is approximated in a short time interval by a low-order differential equation with unknown parts, a so-called ultra-local model. This control method is a powerful tool, but the parametrisation and the concrete implementation may require time, effort, and experience. The present paper investigates the systematic tuning of a model-free controller for a magnetically supported plate that is modelled as an unstable multiple-input multiple-output system. Furthermore, the incorporation of model information into the model-free controller is investigated. These adaptations ultimately improve results by simplifying parameter tuning and interpretation of estimates. Several experiments are carried out on a test bed to show the capabilities of the proposed algorithms for set point stabilisation and trajectory tracking. The effects of the different parameters in the model-free controllers are addressed, and excellent robustness with respect to actuator faults is demonstrated. Filters for estimating derivatives and unknown quantities are designed using an open-source toolbox.

1. Introduction

Model-free control (MFC) has become a popular term in the broad field of control engineering and includes approaches based on proportional integral derivative (PID) control, fuzzy control, reinforcement learning, and data-based control. Fliess and Join (2008, 2009, 2013) have proposed algorithms that do not rely on physically motivated mathematical models of the systems considered and do not require time consuming and data intensive training. In this approach, a system is locally approximated by a low-order differential equation with unknown parts, which is called a ultra-local model. The unknown part of the system consists of unmodelled dynamics as well as disturbances, without any distinction between the latter. With the help of algebraic differentiators (see Mboup et al., 2009 and the survey Othmane et al., 2022 for an overview) the unknown part can be estimated for a subsequent compensation in the feedback control.

This simple yet powerful and real-time capable method has been applied to various systems, ranging from direct fuel injection systems in Carvalho et al. (2024), unmanned aerial vehicles in Al Younes et al. (2014), grid-tied inverters in Wachter et al. (2023), wind turbines in Lafont et al. (2020), active suspensions in Haddar et al. (2019), proportional valves in Scherer et al. (2023), green houses in Lafont

et al. (2015) and video streaming in Fliess and Join (2023), to mention only a small selection of successful simulations and experiments.

The works Li et al. (2022) and Zhang et al. (2022) focus on classical control theoretical tools in the frequency domain to analyse the MFC, whereas Hegedűs et al. (2022) investigates the tuning of the input gain. In Belhadjoudja et al. (2023) the MFC is analysed using methods from linear systems. An alternative MFC approach is considered in Tabuada et al. (2017), where the knee joint of a bipedal walking robot is controlled based on a linear approximation of the nonlinear system with guarantees on stability depending on the sampling time. Nonetheless, systematic tuning of the MFC algorithms for unstable multiple-input multiple-output (MIMO) systems remains a challenging problem, despite the successful realisation in Bekcheva et al. (2018) or Neves and Angélico (2021).

In Othmane, Rudolph, and Mounier (2021) the tuning of estimators used for the approximation of the unknown part of the ultra-local model is investigated. These estimators are called algebraic differentiators, the systematic tuning of which has already been analysed in Kiltz (2017), Kiltz and Rudolph (2013) and Othmane et al. (2022). The design, analysis, and discretisation of the differentiators is done with the easy to use open-source toolbox AlgDiff (see Othmane, 2022), the

---

use of which has been described in the tutorial-like paper (Othmane & Rudolph, 2023).

The present paper focuses on active magnetic bearings. This technology can, for example, be used for flywheels (cf. Lei & Palazzolo, 2008), designed for energy storage, to dampen the vibration of circular saws (Ellis & Mote, 1977), or for the exact positioning of a tool attached to a rotating shaft (Eckhardt & Rudolph, 2004). Due to the inherent nonlinearity and instability in the system, control algorithms are always needed for the realisation of the technology. These algorithms are typically based on mathematical models of the magnets (cf. Collon et al., 2007) and the rigid body dynamics of the rotating shaft. The same technology of the bearings can also be used for the position control of a plate as discussed in Kiltz et al. (2014). The magnetically supported plate described therein is also considered in the present work as an example for the magnetic bearing technology, dealing with interesting problems like over-actuation, nonlinearity of the magnets as well as the unstable MIMO characteristic of the system that is challenging in the MFC context. The contributions De Miras et al. (2013) and Moraes and da Silva (2015) have already successfully described the experimental implementation of MFC techniques for simple lab setups with magnetic bearings. However, questions such as parametrisation, discrete implementation, incorporation of physical knowledge into the controller design, and comparisons with model-based approaches remain open. The current work explores these issues.

Here, the systematic design and tuning of algebraic differentiators and MFC algorithms based on a second order ultra-local model is investigated. The differentiators are essential to online estimate unknown parts of the ultra-local model as well as velocities that are not directly measured but needed for the controller. Additionally, details concerning the implementation of these algorithms are shared that are necessary for a successful application of the latter. It is shown that model information, e.g. known input gains or a simple model of an electromagnet, can be utilised not only to increase the accuracy of the algorithms, but also to simplify the tuning. In addition to the systematic analysis, a model-based approach is designed in such a way that the results of both the MFC and the model-based control (MBC) are comparable. Several experiments on a test bed depicted in Fig. 1 are conducted showing the capabilities of the MFC in different scenarios, such as trajectory tracking and robustness to sensor and actuator faults.

The present paper is organised as follows. In Section 2 the system under consideration is introduced and a mathematical model is provided. A model-based tracking controller, the MFCs using different inputs as well as information concerning the implementation of the latter are discussed in Section 3. In Section 4 experimental results on the test bed are presented and details for the parametrisation of the algorithms are provided.

2. Magnetically supported plate: problem statement and modelling

The test bed considered, depicted in Fig. 1, consists of a 10 mm thick, rectangular aluminium plate with four laminated iron packs at each corner. These packs are acting as the yokes of four electromagnets mounted at a rigid frame above the plate. The electromagnets generate four forces that can lift the plate, as depicted in the schematic drawing in Fig. 2. Four inductive sensors are available to measure the distances denoted by $y_j, j \in \{1, 2, 3, 4\}$, between the plate and the outer frame. This system has already been considered in Kiltz et al. (2014, 2012). Due to its simple construction this setup could be relatively easily rebuilt by other groups for use in educational labs.

2.1. Model of the plate

The plate, as shown in the schematic drawing in Fig. 2, is modelled as a rigid body that can only perform translational motions in the z_0 direction of the space-fixed coordinate system C_0 and tilt around the

Fig. 1. Photo of the considered test bed. The aluminium plate is hovering with an air gap of 5 mm.
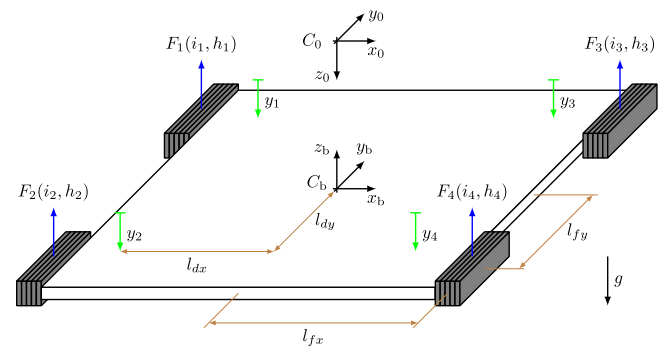

Fig. 2. Schematic drawing of the plate with the body fixed frame C_b and reference frame C_0.

x_b- and y_b-axes of the body-fixed coordinate system C_b, located in the centre of mass of the plate. Thus, motions in any other direction are neglected. Due to the limited air gaps $h_j, j \in \{1, 2, 3, 4\}$, possible tilt angles are small, resulting in the assumption that the forces $F_j, j \in \{1, 2, 3, 4\}$ of the magnets are acting at the centre of each yoke as depicted in Fig. 2. Each force $F_j, j \in \{1, 2, 3, 4\}$ is generated by an electric current denoted by $i_j, j \in \{1, 2, 3, 4\}$. However, the dynamics of the magnetic fields are neglected, because of the lamination of the magnets as well as the current controllers incorporated in the industrial hardware.

Using the latter considerations, the motion of the plate in the remaining three degrees of freedom can be modelled by

$$Bf = mg + P(\ddot{y} - \eta) \tag{1}$$

with

$$B = \begin{pmatrix} 1 & 1 & 1 & 1 \\ 1 & -1 & 1 & -1 \\ 1 & 1 & -1 & -1 \end{pmatrix}, \quad P = \begin{pmatrix} 0 & -\frac{m}{2} & -\frac{m}{2} \\ -\frac{k_1}{2} & \frac{k_1}{2} & 0 \\ -\frac{k_2}{2} & 0 & \frac{k_2}{2} \end{pmatrix},$$

$f = (F_1, F_2, F_3, F_4)^{\mathrm{T}}$, $y = (y_1, y_2, y_3)^{\mathrm{T}}$, $g = (g, 0, 0)^{\mathrm{T}}$, and the parameters $k_1 = \frac{J_x}{l_{dy}l_{fy}}$ and $k_2 = \frac{J_y}{l_{dx}l_{fx}}$. The mass of the plate is denoted by m, the gravitational acceleration by g, J_x and J_y are describing the moments of inertia with respect to the x_b- and y_b-axes respectively. As depicted in Fig. 2, the distances from the centre of the plate to the sensors and the forces are denoted by l_{dx} and l_{dy} as well as l_{fx} and l_{fy}, respectively. Unmodelled system dynamics and disturbances are summarised in the variable η.

As usual, the forces generated by the magnets are modelled as

$$F_j = \frac{i_j^2}{d_j^2(h_j)}, \quad j \in \{1,2,3,4\}, \tag{2}$$

with functions $d_j : \mathbb{R} \to \mathbb{R}$ depending on the air gaps $h_j, j \in \{1,2,3,4\}$. These functions can be determined in a parameter identification with an appropriate ansatz. In the following, the air gaps $h_j, j \in \{1,2,3,4\}$, have to be calculated using the available measurements. The easiest way of doing so is to use the assumption that the aluminium plate is a rigid body. Then it can be mathematically described by a plane defined by

$$\boldsymbol{r}^0 = \boldsymbol{r}_1^0 + a(\boldsymbol{r}_3^0 - \boldsymbol{r}_1^0) + b(\boldsymbol{r}_2^0 - \boldsymbol{r}_1^0) \tag{3}$$

in the reference frame C_0 with the sensor locations $\boldsymbol{r}_1^0 = (-l_{dx}, l_{dy}, y_1)^\mathrm{T}$, $\boldsymbol{r}_2^0 = (-l_{dx}, -l_{dy}, y_2)^\mathrm{T}$, and $\boldsymbol{r}_3^0 = (l_{dx}, l_{dy}, y_3)^\mathrm{T}$, whereas the parameters a and b depend on the point of interest on the plane. With this, only three of the four sensor values have to be used. Now, (3) can be used to calculate the midpoint of the yokes, where the forces of the magnets are acting on, and with this the needed air gaps. This yields

$$\begin{pmatrix} h_1 \\ h_2 \\ h_3 \\ h_4 \end{pmatrix} = \frac{1}{2} \begin{pmatrix} k_x+k_y & 1-k_y & 1-k_x \\ k_x-k_y & 1+k_y & 1-k_x \\ -k_x+k_y & 1-k_y & 1+k_x \\ -k_x-k_y & 1+k_y & 1+k_x \end{pmatrix} \begin{pmatrix} y_1 \\ y_2 \\ y_3 \end{pmatrix} = K\boldsymbol{y}, \tag{4}$$

with $k_x = \frac{l_{fx}}{l_{dx}}$ and $k_y = \frac{l_{fy}}{l_{dy}}$, which maps the sensor values to the air gaps.

Remark 1. The term $\boldsymbol{\eta}$ describes several hard to model dynamics and disturbances. These have various origins, such as errors within the magnetic force model stemming from inaccuracies in the functions $d_j : \mathbb{R} \to \mathbb{R}, j \in \{1,2,3,4\}$, unmodelled hysteresis and magnetic saturation, temperature dependencies within the coils, effects originating from magnetic field dynamics, and magnetic flux leakage. Additionally, high-frequency oscillations occur due to plate vibrations, as the real plate deviates from the assumed rigid body model.

Remark 2. Using a different combination of three sensor values would be possible, e.g. y_2, y_3, and y_4. In this case, Eq. (3) has to be adjusted, resulting in a different matrix relating $\boldsymbol{h}$ and $(y_2, y_3, y_4)^\mathrm{T}$. A possible method of using four sensors is to calculate the centre of gravity of the plate, where the coordinate system C_b is located, as the mean value of all measurements. The tilt angles around the x_b- and y_b-axes can be calculated afterwards using again only three sensor values, and with this all informations to determine the air gaps are provided. An other possibility is to use the redundancy of the sensors for fault detection. For the sake of simplicity, only the suggested choice is considered in the sequel.

3. Control design

In the following section, a MBC approach is presented in addition to several MFC algorithms, which differ in the choice of the input. This choice is based on different degrees of model information used to determine a feedback law.

3.1. Model-based control

The MBC of the plate is based on (1), which can be rewritten as

$$\ddot{\boldsymbol{y}} = P^{-1}(B\boldsymbol{f} - m\boldsymbol{g}) + \boldsymbol{\eta} \tag{5}$$
$$= \boldsymbol{v} + g\,(1 \quad 1 \quad 1)^\mathrm{T} + \boldsymbol{\eta},$$

with the new input $\boldsymbol{v} = P^{-1}B\boldsymbol{f}$. The latter system of differential equations can also be written as three independent scalar equations

$$\ddot{y}_k = v_k + g + \eta_k, \quad k \in \{1,2,3\}. \tag{6}$$

Hereafter, the index k will be omitted, due to the similarity of the equations. Based on (6) a stabilising feedback law

$$v = \ddot{y}_\mathrm{r} - c_\mathrm{D}\dot{e} - c_\mathrm{P}e - g - \eta, \quad e = y - y_\mathrm{r}, \tag{7}$$

can be calculated to track a sufficiently smooth reference trajectory $t \mapsto y_\mathrm{r}(t)$. Using the control law (7) on system (6) leads to the differential equation of the error

$$\ddot{e} + c_\mathrm{D}\dot{e} + c_\mathrm{P}e = 0. \tag{8}$$

The controller parameters c_P and c_D are chosen positive, which results in a stable closed-loop behaviour. This approach can be interpreted as a typical flatness-based controller as discussed e.g. in Rudolph (2021).

Since the velocity $\dot{y}$ and the acceleration η required in the feedback law (7) are not measured, an observer is designed, based on the assumption of a piecewise constant disturbance η, which means $\dot{\eta} = 0$ on intervals. To this end, the state representation of (6) can be introduced as

$$\dot{\boldsymbol{x}} = \begin{pmatrix} 0 & 1 & 0 \\ 0 & 0 & 1 \\ 0 & 0 & 0 \end{pmatrix} \boldsymbol{x} + \begin{pmatrix} 0 \\ 1 \\ 0 \end{pmatrix}(v+g) = A\boldsymbol{x} + \boldsymbol{b}(v+g) \tag{9a}$$

$$y = (1 \quad 0 \quad 0)\,\boldsymbol{x} = \boldsymbol{c}^\mathrm{T}\boldsymbol{x} \tag{9b}$$

with the input v and the tuple $\boldsymbol{x} = (y, \dot{y}, \eta)^\mathrm{T}$. Discontinuities of η correspond to resetting initial conditions. Based on (9) a simple linear disturbance observer

$$\dot{\hat{\boldsymbol{x}}} = A\hat{\boldsymbol{x}} + \boldsymbol{b}(v+g) + \boldsymbol{l}\left(y - \boldsymbol{c}^\mathrm{T}\hat{\boldsymbol{x}}\right) \tag{10}$$

with $\hat{\boldsymbol{x}}(0) = \hat{\boldsymbol{x}}_0 \in \mathbb{R}^3$ provides an estimate $\hat{\boldsymbol{x}}$ of the tuple $\boldsymbol{x}$. The observer gains $\boldsymbol{l} = (l_1, l_2, l_3)$ are chosen such that $A - \boldsymbol{l}\boldsymbol{c}^\mathrm{T}$ is Hurwitz. With this choice the error $\tilde{\boldsymbol{x}} = \boldsymbol{x} - \hat{\boldsymbol{x}}$ exponentially converges to zero. Using the feedback law (7) in combination with the observer (10) the accelerations $\boldsymbol{v}$ can be calculated.

The next step is to exploit the relation $\boldsymbol{v} = P^{-1}B\boldsymbol{f}$ from (5) to derive desired forces $\boldsymbol{f}_\mathrm{d}$ that can be realised using the electric currents. Due to the redundancy stemming from the over-actuation of the system, a choice has to be made. One approach is to use the Moore–Penrose pseudo inverse $B^\dagger = B^\mathrm{T}(BB^\mathrm{T})^{-1}$ of B to calculate

$$\boldsymbol{f}_\mathrm{d} = B^\dagger P\boldsymbol{v} = \frac{1}{4} \begin{pmatrix} \frac{-k_1-k_2}{2} & \frac{-m+k_1}{2} & \frac{-m+k_2}{2} \\ \frac{k_1-k_2}{2} & \frac{-m-k_1}{2} & \frac{-m+k_2}{2} \\ \frac{-k_1+k_2}{2} & \frac{-m+k_1}{2} & \frac{-m-k_2}{2} \\ \frac{k_1+k_2}{2} & \frac{-m-k_1}{2} & \frac{-m-k_2}{2} \end{pmatrix} \boldsymbol{v} = V\boldsymbol{v} \tag{11}$$

that distributes the input $\boldsymbol{v}$ evenly to the four desired forces $F_{\mathrm{d},j}, j \in \{1,2,3,4\}$, which is beneficial especially if an abrupt actuator fault occurs, as discussed in Section 4.4.1.

Remark 3. Using the Moore–Penrose pseudo inverse is equivalent to minimising the mean variation $\sum_{i=1}^4 \left(F_{\mathrm{d},i} - \frac{1}{4}\sum_{j=1}^4 F_{\mathrm{d},j} \right)^2$ as suggested in Kiltz et al. (2012).

Solving (2) for the current yields

$$i_{\mathrm{d},j} = \sqrt{F_{\mathrm{d},j}}\, d_j(h_j), \quad j \in \{1,2,3,4\}, \tag{12}$$

which can be used together with (4) to generate the reference for the underlying current controller.

3.2. Model-free control

In the following, various MFC approaches are presented, gradually reducing from one subsection to the next the amount of physically motivated model knowledge. For each controller three decoupled systems with identical structure are considered and the corresponding index will again be dropped when appropriate.

3.2.1. Acceleration as input

Hereafter, the input v is used just as it has been done in the design of the MBC law in (7). Each of the decoupled subsystems is described by

$$\ddot{y} = \gamma_v v + f_v, \quad \gamma_v > 0, \tag{13}$$

where $t \mapsto f_v(t)$ is a bounded unknown square-integrable function representing unmodelled dynamics as well as other disturbances. Comparing (13) and (6) yields $f_v = \eta + g$ and suggests the choice $\gamma_v = 1$. This means that f_v has a physical meaning as opposed to a similar case study discussed in Remark 3 of Scherer et al. (2023).

Remark 4. Comparing (13) and (6) suggests to use $\gamma_v = 1$. Nevertheless, a different choice of the input gain γ_v is possible (see Fig. 8).

Based on (13), the control input v is chosen as

$$v = \frac{1}{\gamma_v} \left(\ddot{y}_{\mathrm{r}} - k_{\mathrm{p}} e - k_{\mathrm{d}} \dot{e} - \hat{f}_v \right) \tag{14}$$

with $k_{\mathrm{p}}, k_{\mathrm{d}} > 0$, and estimates $\hat{f}_v$ and $\hat{\dot{y}}$ of f_v and $\dot{y}$, respectively, the calculation of which will be discussed in Section 3.3. Under the assumption that $\hat{f}_v \approx f_v$, using (14) with the model (13) leads to the differential equation

$$\ddot{e} + k_{\mathrm{d}} \dot{e} + k_{\mathrm{p}} e = 0,$$

which has the same structure as (8).

The controller (14) can then be used together with (4), (11) and (12) to calculate the desired forces and currents, respectively. An advantage of this implementation is that there is no need for a model-based observer to estimate the derivative $\dot{y}$ and the disturbance f_v. Instead, with the algebraic differentiators presented in Appendix A, an approach that is solely based on the measured signal y is used.

Remark 5. This combination of MBC and MFC is also suggested in Villagra and Herrero-Pérez (2012). Therein the MFC is combined with a nonlinear flatness-based control.

3.2.2. Magnetic force as input

Instead of choosing the acceleration v as an input, it is possible to directly calculate the magnetic forces $\tilde{F}_k, k \in \{1, 2, 3\}$. Based on this consideration, the model (5) can be written as

$$\ddot{y}_k = -\rho F_k - \varpi_k(F_{\neq k}) + g + \eta_k, \tag{15}$$

with $F_{\neq k} = \{F_1, F_2, F_3, F_4\} \backslash \{F_k\}$, where $\varpi_k(F_{\neq k})$ is a weighted sum of the different magnetic forces acting on the plate and the parameter $\rho = 1/k_1 + 1/k_2 + 1/m$ resulting from $P^{-1}B$. The structure of (15) leads to ultra-local models

$$\ddot{y}_k = f_{\tilde{F},k} - \gamma_{\tilde{F}} \tilde{F}_k, \quad \gamma_{\tilde{F}} > 0, \tag{16}$$

with $\gamma_{\tilde{F}} = \rho$ and the unknown parts are $f_{\tilde{F},k} = \varpi_k(F_{\neq k}) + g + \eta_k$. With (15) in mind, (16) can be interpreted as a model of three implicitly coupled point masses.

Remark 6. As an alternative to the considerations based on the model (5), assuming that there is no unknown part $f_{\tilde{F}}$, the model (16) would be $\ddot{y} = -\gamma_{\tilde{F}} \tilde{F}$. The force $\tilde{F}$ and the parameter $\gamma_{\tilde{F}}$ are assumed to be always positive, which means that if the force is increased the acceleration $\ddot{y}$ is negative and the resulting position y will decrease. This matches the physical behaviour, because the air gap of the magnet is getting smaller if the force is increased and the magnet pulls the plate towards the rigid outer frame.

A controller that directly commands the forces is

$$\tilde{F} = \frac{1}{\gamma_{\tilde{F}}} \left(-\ddot{y}_{\mathrm{r}} + k_{\mathrm{p}} e + k_{\mathrm{d}} \dot{e} + \hat{f}_{\tilde{F}} \right), \tag{17}$$

where the estimate $t \mapsto \hat{f}_{\tilde{F}}(t)$ is derived according to (24) by substituting v with $\tilde{F}$.

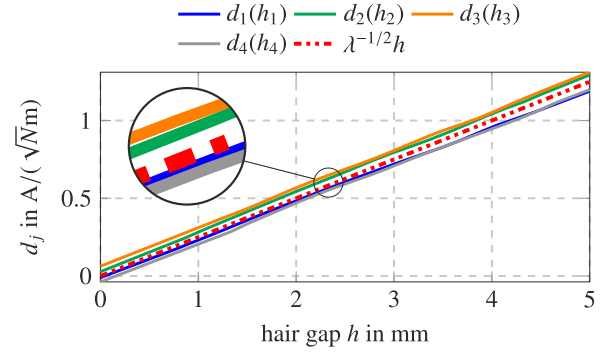**Fig. 3.** Graphical representation of the identified functions $d_j(h_j), j \in \{1, 2, 3, 4\}$ and the approximation with the parameter λ used to further simplify the design of the MFC approach.

Again, the remaining degree of freedom, caused by the over-actuation of the system, has to be considered. The transformation resulting from the pseudo inverse is not a valid solution for this. To see this, assuming the plate hovers horizontally with a constant distance to the frame. Then, the available forces have to compensate the gravitational forces and are approximately equal to $\tilde{F}_k \approx \bar{F} > 0, k \in \{1, 2, 3\}$. In this case, the last row of the pseudo inverse reads $F_{\mathrm{d},4} = \frac{1}{4}(\tilde{F}_1 - \tilde{F}_2 - \tilde{F}_3) = -\frac{1}{4}\bar{F}$, which cannot be realised on the test bed because the magnetic forces $F_j, j \in \{1, 2, 3, 4\}$ are restricted to positive values. Instead of directly coupling all forces, one can use $F_{\mathrm{d},k} = \tilde{F}_k, k \in \{1, 2, 3\}$ and get the remaining force as

$$F_{\mathrm{d},4} = \sum_{k=1}^{3} a_k \tilde{F}_k, \tag{18}$$

with $\sum_{k=1}^{3} a_k = 1$ and $a_k \geq 0$. Thereafter, (4) and (12) can again be used to calculate the desired electrical currents.

3.2.3. New input $u = (i/h)^2$

To further simplify the design of the MFC, the functions $d_j : \mathbb{R} \to \mathbb{R}$ in (2) can be approximated with $d_j \approx \lambda^{-1/2} h_j, j \in \{1, 2, 3, 4\}, \lambda > 0$, as depicted in Fig. 3, which results in

$$F \approx \lambda \left(\frac{i}{h} \right)^2 = \lambda u.$$

Considering this relation, the quantity $u = (i/h)^2$ is chosen as a new input and can be interpreted as a special case of the considerations from Section 3.2.2.

Thus, according to the model (16) it follows that

$$\ddot{y} = f_u - \gamma_u u,$$

with $\gamma_u = \lambda \gamma_{\tilde{F}}$. The control input u can be derived using (17) and by substituting $\tilde{F}$ and $\gamma_{\tilde{F}}$ with u and γ_u, respectively, which yields

$$u = \frac{1}{\gamma_u} \left(-\ddot{y}_{\mathrm{r}} + k_{\mathrm{p}} e + k_{\mathrm{d}} \dot{e} + \hat{f}_u \right). \tag{19}$$

As described in Section 3.2.2 the estimation of f_u is realised according to (24) by substituting v with u. Similar to (18) the remaining input u_4 can be calculated. Finally, using $i_{\mathrm{d},j} = \sqrt{u_j} h_j, j \in \{1, 2, 3, 4\}$ together with (4), the desired currents for the underlying current controller are obtained.

Remark 7. From an engineering perspective the input u is a reasonable choice if no identified model of the force (2) is available. From a physical understanding of the system it is known that the force of the magnets is approximately proportional to $(i/h)^2$.

3.2.4. Current as input

Using even less model information, the equation

$$\ddot{y} = f_i - \gamma_i(y)i \tag{20}$$

can be assumed to describe the system. In this case, however, the input gain

$$\gamma_i(y) = \frac{\gamma_{i,0}}{y}$$

is a function of the position, with $\gamma_{i,0} > 0$, obviously inspired by the input u from Section 3.2.3. For the implementation of this gain the singularity of γ_i is not an issue, because of a safety routine that limits the air gaps $h_j, j \in \{1, 2, 3, 4\}$ to a minimum of $0.8\,\text{mm}$. The MFC law can be derived as

$$i = \frac{1}{\gamma_i(y)} \left(-\ddot{y}_\text{r} + k_\text{p}e + k_\text{d}\dot{e} + \hat{f}_i \right), \tag{21}$$

and again the estimation of f_i is realised by substituting v with i in (24). The additional input can be derived as in (18).

Remark 8. Choosing a constant input gain in (20) works in simulation, but it was not leading to a stable closed-loop behaviour on the test bed.

3.3. Implementation of the MFC algorithms

In the following section, details about the implementation of the MFC are shared. For additional information about the algebraic differentiators used in the implementation of the proposed algorithms, the interested reader is referred to Appendix A and the references therein.

3.3.1. Estimation of the disturbance f

The proposed MFC algorithms, i.e. (14), (17), (19) and (21), are designed for continuos-time systems. Nevertheless, for a discrete-time realisation of the control algorithms, a evaluation at equidistant time instants is needed. In the following the MFC law (14) will be considered as an example, but all remarks can be applied to the other approaches in a similar way.

Estimation of f_v can be done with

$$\hat{f}_v(t) = \frac{5!}{2T^5} \int_{t-T-\varepsilon}^{t-\varepsilon} \left(T^2 - 6T\sigma + 6\sigma^2 \right) y(\tau) - \frac{\gamma_v}{2}\sigma^2(T-\sigma)^2 v(\tau) \mathrm{d}\tau, \tag{22}$$

where $\sigma = t - \tau - \varepsilon$ and $\varepsilon > 0$, which is based on algebraic considerations and commonly used in the literature, e.g. Bekcheva et al. (2018) or Barth et al. (2020). In Appendix B it is shown that (22) can be interpreted as

$$\hat{f}_v(t) = \int_{t-T-\varepsilon}^{t-\varepsilon} \ddot{g}_{0,T,\vartheta}^{(2,2)}(t-\tau-\varepsilon)y(\tau) - \gamma_v g_{0,T,\vartheta}^{(2,2)}(t-\tau-\varepsilon)v(\tau)\mathrm{d}\tau. \tag{23}$$

In the latter $g_{0,T,\vartheta}^{(2,2)}$ denotes an algebraic differentiator as first developed in Mboup et al. (2009), using here the notation from Othmane et al. (2022) with the parameters $\alpha = \beta = 2$ and $N = 0$. With these considerations, (23) can thus be generalised to

$$\hat{f}_v(t) = \int_{t-T-\varepsilon}^{t-\varepsilon} g(t-\tau-\varepsilon)f(\tau)\mathrm{d}\tau, \tag{24a}$$

$$= \int_{t-T-\varepsilon}^{t-\varepsilon} \ddot{g}(t-\tau-\varepsilon)y(\tau) - \gamma_v g(t-\tau-\varepsilon)v(\tau)\mathrm{d}\tau, \tag{24b}$$

where $g = g_{N,T,\vartheta}^{(\alpha,\beta)}$ is the algebraic differentiator with parameters as discussed in Appendix A. As seen in Section 4, in some cases this generalisation is needed to realise the MFC.

The convolution integrals in (24b) have to be approximated using a suitable quadrature method. The open-source toolbox AlgDiff (see Othmane, 2022) provides all necessary features for the design and analysis as well as the discretisation of algebraic differentiators used for the estimation of f_v and the time derivatives of y. The tutorial Othmane and Rudolph (2023) offers an introduction with examples to the toolbox and the systematic parametrisation of these differentiators.

As discussed in Scherer et al. (2023), the formulation in (24b) can be derived by integrating (24a) by parts using (13). Again (24b) can be implemented, because it depends on quantities known in the interval $[t - T - \varepsilon, t - \varepsilon]$ only.

In the following, the time window of length T is an integral multiple of the sampling time t_s, i.e. $T = n_\text{s}t_\text{s}$ and the parameter ε in (24) is chosen to be equal to t_s. The abbreviation $v[k] = v(kt_\text{s}), k \in \mathbb{N}$ is used for v evaluated at the time kt_s. With this abuse of notation, (14) yields in a discrete-time setting

$$v[k] = \frac{1}{\gamma_v} \left(\ddot{y}_\text{r}[k] - k_\text{p}\hat{e}[k] - k_\text{d}\dot{\hat{e}}[k] - \hat{f}_v[k] \right) \tag{25}$$

with $\hat{e}^{(n)}[k] = \hat{y}^{(n)}[k] - y_\text{r}^{(n)}[k], n \in \{0, 1\}$. Applying the mid-point rule, $\hat{f}_v$ and the estimates of the derivatives $y^{(n)}, n \in \{0, 1\}$ can be computed as

$$\hat{f}_v[k] = \frac{1}{\Phi_2} \sum_{j=0}^{L-1} w_2[j]y[k-j-1] - \frac{\gamma_v}{\Phi_0} \sum_{j=0}^{L-1} w_0[j]v[k-j-1]$$

$$\hat{y}^{(n)}[k] = \frac{1}{\Phi_n} \sum_{j=0}^{L-1} w_n[j]y[k-j],$$

with $\Phi_n = \frac{t_\text{s}^n}{n!} \sum_{j=0}^{L-1} w_n[j](-j)^n$, $w_n[j] = t_\text{s}g^{(n)}[j+1/2]$, $n \in \{0, 1\}$, and $L = n_\text{s}$.

4. Experimental results

The following, experiments are carried out on the test bed depicted in Fig. 1. Four inductive sensors manufactured by Intronik GmbH are measuring the distance between the rigid outer frame and the $4.69\,\text{kg}$ weighing aluminium plate. For safety reasons, the air gaps $h_j, j \in \{1, 2, 3, 4\}$ of the magnets are limited to $0.8 - 5.5\,\text{mm}$ and the currents to $0 - 8\,\text{A}$. The real-time hardware used is a GIN-SAM3 from Indel. The proposed algorithms are executed with a sampling rate of $f_\text{s} = 1/t_\text{s} = 32\,\text{kHz}$. The power electronics are included in a GIN-SAC3x3 also from Indel.

4.1. Parameters of algebraic differentiators and MFC

The algebraic differentiators used depend on the design parameters α, β, N, and ω_c that have to be chosen in such a way that the accuracy of the resulting approximation as well as the rejection of measurement noise are high and the error stemming from the delay δ_t is as small as possible (see Appendix A for more information about the algebraic differentiators used). To achieve a high noise rejection the parameters α and β are chosen equal (see Othmane et al., 2022, Sec. 4 and Mboup & Riachy, 2018). Additionally the parameter N describing an N-th order truncated generalised Fourier expansion is set to zero, thus, resulting in an estimation delay of $\delta_t = T/2$.

With these choices, several experiments are made using different parameter combinations for $\alpha = \beta \in \{2, 3, \dots, 8\}$ and $\omega_\text{c} \in \{540, 640, \dots, 1440\}$ rad/s. The MFC from (14) is implemented with the parameters $k_\text{p} = 5000\,\text{s}^{-2}, k_\text{d} = 195\,\text{s}^{-1}$ and $\gamma_v = 1$. At the beginning, the plate rests on four screws at a distance of approximately $5.5\,\text{mm}$ and individual polynomial reference trajectories $t \mapsto y_{\text{r},k}(t), k \in \{1, 2, 3\}$ of degree 5 are planned, connecting the rest position with a vertical position at $2\,\text{mm}$ and a transition time of $2\,\text{s}$. If the algorithm can lift and afterwards stabilise the plate, the experiment will continue, otherwise it is aborted. Thereafter, a set point transition from $2\,\text{mm}$ to $5\,\text{mm}$ and back again to $2\,\text{mm}$ with polynomial trajectories of degree 5 are calculated, having a transition time of $0.5\,\text{s}$ as well as a holding time of $0.2\,\text{s}$ (see Fig. 11 for a visualisation of the reference trajectory).

For this set point change, the root mean square (RMS) of the delayed errors $\hat{e}_k = \hat{y}_k - y_{\text{r},k}, k \in \{1, 2, 3\}$, is calculated and used as a quality gauge of the resulting parametrisation. Fig. 4 shows the variation of the RMS values of the errors for different combinations of the parameters $\alpha = \beta$ and ω_c. The experiments show that the RMS values are
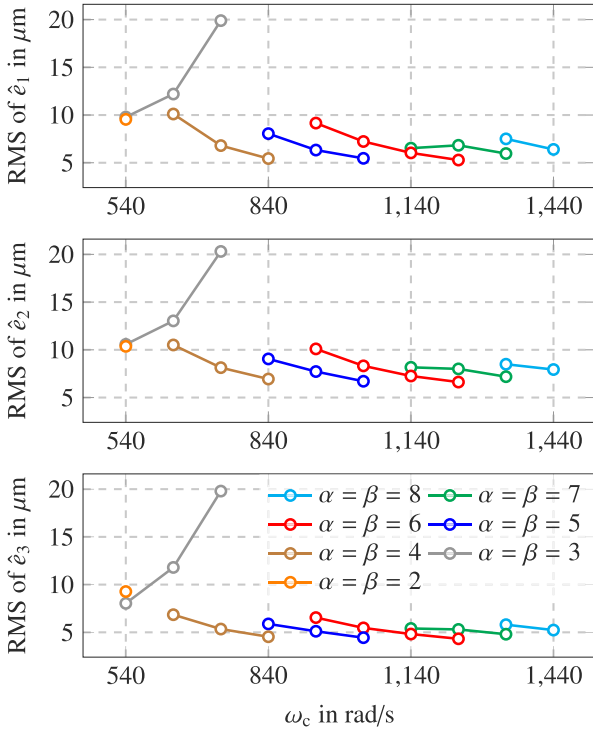
Fig. 4. Evaluating the RMS values of the delayed error $\hat{e}_k, k \in \{1, 2, 3\}$ for varying parameter combinations of ω_c and $\alpha = \beta$ for the algebraic differentiators.

Table 1
Comparison of the cost function values $\mathcal{J}_2$ for $\omega_c = 840 \, \text{rad/s}$ and varying $\alpha = \beta$ with the discretisation methods used.

Method	$\alpha = \beta = 2$	$\alpha = \beta = 3$	$\alpha = \beta = 4$
mid-point	−67.1 dB	−130.6 dB	−222.1 dB
trapezoidal	−56.5 dB	−120.7 dB	−220.7 dB
Simpson's rule	−22.5 dB	−33.4 dB	−31.2 dB

significantly larger for $\alpha = \beta \in \{2, 3\}$ compared to the results of the experiments for $\alpha = \beta > 3$. This confirms the general choice of the formulation with algebraic differentiators in e.g. (14) compared to the restriction to $\alpha = \beta = 2$ as discussed in Appendix B, at least for the current application. The large discretisation error is the reason for the results from Fig. 4, which can be seen in Fig. 5, where the amplitude spectra of the continuous-time and discrete-time differentiators used for the approximation of a second order derivative are depicted for the choice $\omega_c = 840 \, \text{rad/s}$, $N = 0$, and varying $\alpha = \beta$. The differentiator has been discretised using the mid-point rule. Specifically, for very low frequencies compared to ω_c the estimation of $\ddot{y}$ is bad, resulting in an inaccurate estimation and compensation of f_v in the controller. Using the cost function $\mathcal{J}_n$ introduced in Kiltz (2017, Sec. 3.4.2) and discussed in Othmane et al. (2022), as a measure for the discretisation reveals that for values above -200 dB the discretisation error is unacceptable. In Table 1 results obtained using the mid-point rule, the trapezoidal rule and Simpson's rule for the discretisation are compared. The comparison shows that the trapezoidal rule or Simpson's rule result in even higher values for $\mathcal{J}_n$. Therefore, the mid-point rule is used in the sequel. In addition, using the latter, fewer filter parameters have to be stored and fewer calculations have to be done as discussed in Kiltz (2017, Sec. 3.4.2) or Othmane, Rudolph, and Mounier (2021, Sec. 3.3).

Remark 9. The plate has a dominant mechanical resonance frequency at approximately 942 rad/s, which causes instability of the closed loop if not suppressed correctly. Choosing $N = 0$ and $\alpha = \beta$, the amplitude spectrum of the algebraic differentiator shows a distinct stopband
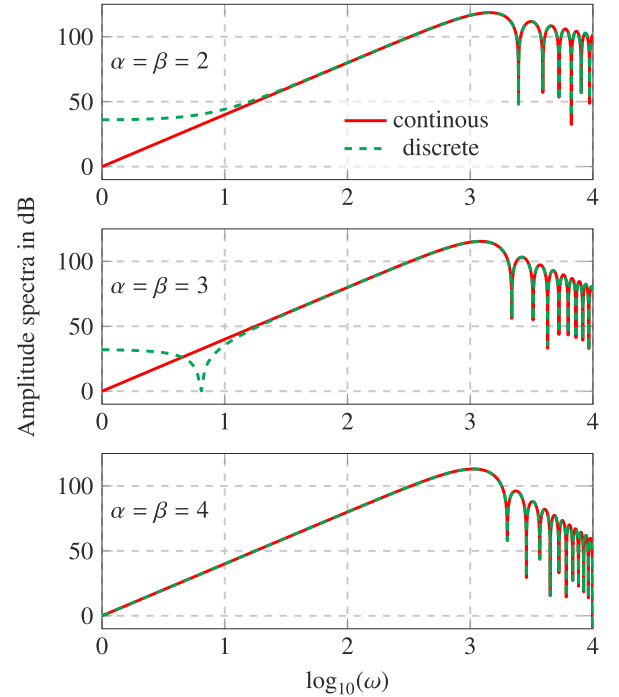

Fig. 5. Comparison of the amplitude spectra of the continuous-time and discrete-time differentiators used for the approximation of a second order derivative for different $\alpha = \beta$ and $\omega_c = 840 \, \text{rad/s}$. The mid-point rule is considered in the discretisation, the corresponding error of which is dominant for $\alpha = \beta \in \{2, 3\}$, resulting in a bad estimation of the second order derivative of $y_k, k \in \{1, 2, 3\}$.

ripple, as depicted in Fig. 5. In this case, the transfer function has zeros which correspond to those of the Bessel function of the first kind and order $\alpha + 1/2$ as mentioned in Kiltz and Rudolph (2013) or Kiltz (2017, Sec. 3.3.3). Because of the sampling in combination with the logarithmic scale of the plot these zeros are not correctly displayed in Fig. 5. Nevertheless, this property can be used to design filters that have the same effect as a notch filter. Unfortunately, in this case, it is not suitable to use this effect for the dominant mechanical resonance frequency. The reason for this is the large window length T resulting in a computational burden that is too high for the computational capabilities of the hardware used. Therefore, a conventional notch filter will later be used to suppress this frequency.

The available computation time of the real-time hardware used is limited. Therefore, some parameter combinations, e.g. $\omega_c = 540 \, \text{rad/s}$ and $\alpha = \beta = 8$, required large filter window lengths which are not realisable since the computation time becomes too large. The parameter range covered is depicted in Fig. 6 . Green and red squares are marking the parameter combinations resulting in a stable and unstable closed-loop behaviour, respectively. Parameter combinations marked with a black square are unrealisable with the hardware used. It is noticeable that Fig. 6 shows some kind of pattern for a stable and realisable combination. Nevertheless, the discretisation error is not the reason for this pattern, because it mainly effects combinations with $\alpha = \beta \in \{2, 3\}$. The origin of this phenomenon is still up to further investigation.

For the following experiments, the parametrisation $\alpha = \beta = 4$ and $\omega_c = 840 \, \text{rad/s}$ is chosen, because according to Fig. 4, this combination has resulted in the smallest RMS values.

With γ_v, k_p, and k_d, the MFC law (14) has three parameters that have to be chosen. As discussed in Remark 4, the model (6) suggests $\gamma_v = 1$, which leaves only two parameters to vary. Fig. 7 shows a parameter sweep in the k_p-k_d-plane carried out on the test bed. Every mark represents a unique parameter combination and an experiment that was made. The maximal currents as well as the RMS values in
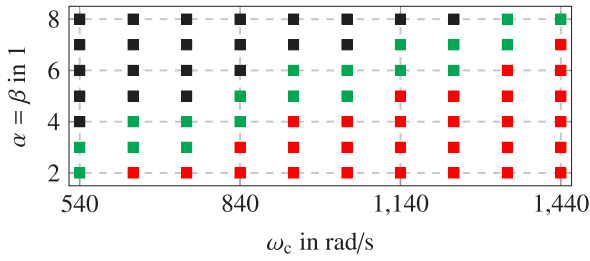
Fig. 6. Visualisation of the different parameters $\omega_c \in \{540, 640, \ldots, 1440\}$ rad/s and $\alpha = \beta \in \{2, 3, \ldots, 8\}$ for the algebraic differentiators covered. Green and red squares are marking the parameter combinations resulting in a stable and unstable closed-loop behaviour, respectively. Parameter combinations marked with a black square are unrealisable with the hardware used. (For interpretation of the references to colour in this figure legend, the reader is referred to the web version of this article.)
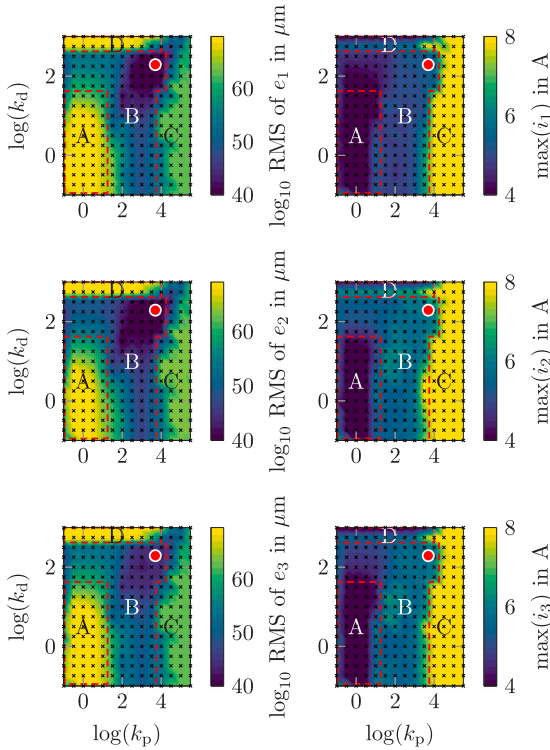

Fig. 7. Results of the parameter sweep of the MFC from (14) with $\gamma_v = 1$, to determine stable tracking behaviour. The red dot marks the parameter combination $k_p = 5000\,\mathrm{s}^{-2}$ and $k_d = 195\,\mathrm{s}^{-1}$ used for further experiments. (For interpretation of the references to colour in this figure legend, the reader is referred to the web version of this article.)

dB of each error $e_k, k \in \{1, 2, 3\}$ are shown. In the region marked with A the RMS values are high and the maximal current is not exceeding 4.2 A, which is not enough to even lift the plate, whereas region C shows the maximum current of 8 A and also high RMS values. For parameter combinations in this region the feedback is not resulting in a stable closed-loop behaviour. Between these two areas, in the region marked with B, the combinations result in low error values and a medium current. There, the closed loop is stable and a local optimum of the RMS values can be found. For the experiments in region D, the maximal current is low but the RMS values are high. This is because the aforementioned safety routine has been activated and the experiment was aborted. In this region the MFC cannot achieve a stable closed loop.

For further experiments the choice $k_p = 5000\,\mathrm{s}^{-2}$ and $k_d = 195\,\mathrm{s}^{-1}$ is made, because according to Fig. 7 (see the red dot) this combination is near a minimum of all three RMS values.
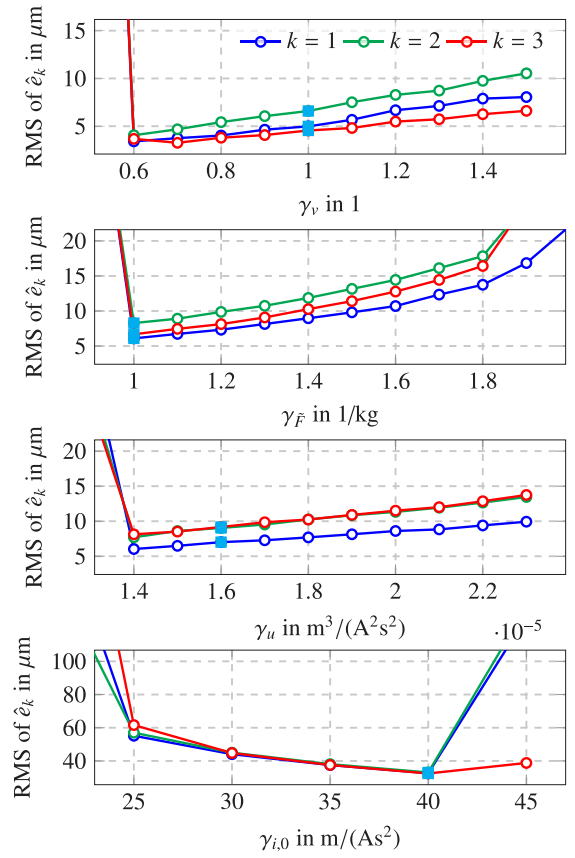

Fig. 8. Parameter sweep of the input gains γ_v, $\gamma_{\tilde{F}}$, γ_u and γ_i with fixed $k_p = 5000\,\mathrm{s}^{-2}$ and $k_d = 195\,\mathrm{s}^{-1}$ to validate the suggestions made by the mathematical model (1). The blue square is marking the parameter used for further experiments. (For interpretation of the references to colour in this figure legend, the reader is referred to the web version of this article.)

Based on the model (1) and (2), several choices for the input gains $\gamma_j, j \in \{v, \tilde{F}, u, i\}$ have been discussed in Section 3. Therefore, the proposed algorithms are verified by performing experiments using various parameter combinations. Fig. 8 shows that with a value of $\gamma_v = 0.6$ the lowest RMS value could be obtained. Nevertheless, $\gamma_v = 1$ is chosen to compare the results with the MBC algorithm. A value of 0.5 is resulting in an unstable closed loop. This shows that the choice of the input gain has also an influence on the stability of the MFC. According to (15) and the model parameters summarised in Table 2, $\gamma_{\tilde{F}} = 0.84\,\mathrm{kg}^{-1}$ is a suitable choice. Unfortunately, this combination is resulting in an unstable closed-loop behaviour on the test bed. This observation might point to model errors. For that reason, $\gamma_{\tilde{F}} = 1\,\mathrm{kg}^{-1}$. As explained in Section 3.2.3, with the choice of $\gamma_{\tilde{F}} = 1\,\mathrm{kg}^{-1}$ and the parameter $\lambda^{-1/2} = 250\,\mathrm{As}/(\mathrm{kgm}^3)^{\frac{1}{2}}$ stemming from the identification of the force model, $\gamma_u = 1.6^{-5}\,\mathrm{m}^3/(\mathrm{A}^2\mathrm{s}^2)$. Again Fig. 8 shows that with a value of $1.4^{-5}\,\mathrm{m}^3/(\mathrm{A}^2\mathrm{s}^2)$ a better result can be obtained, but for the sake of comparison this value is not chosen. For the MFC law (21) the input gain is set to $\gamma_{i,0} = 40\,\mathrm{m}/(\mathrm{As}^2)$. This choice is made only according to Fig. 8, because no model information can be used in this case.

For the MFC algorithms (17), (19), and (21) the free parameter is set to $F_{d,4} = \frac{1}{2}(\tilde{F}_2 + \tilde{F}_3)$ and similarly for u and i.

4.2. Implementation of the MBC

The goal of the following section is to tune the MBC in such a way that it is suitable for a fair comparison with the proposed MFC

Table 2
Parameters of the model (1) used for the MBC.

Param.	Value	Param.	Value
J_x	$5.13 \cdot 10^{-2}\,\mathrm{kgm^2}$	m	$4.69\,\mathrm{kg}$
J_y	$8.19 \cdot 10^{-2}\,\mathrm{kgm^2}$	g	$9.81\,\mathrm{m/s^2}$
l_{dx}	$135\,\mathrm{mm}$	l_{fx}	$182.5\,\mathrm{mm}$
l_{dy}	$144\,\mathrm{mm}$	l_{fy}	$117\,\mathrm{mm}$

algorithms. Table 2 summarises the model parameters required by the MBC law in (7), (11), and (12). The gains $c_P = 5000\,\mathrm{s^{-2}}$ and $c_D = 195\,\mathrm{s^{-1}}$ of the MBC are chosen such that they match the parameters k_p and k_d of the MFC. The control law is implemented in a quasi-continuous manner, which means that the control inputs are sampled and held.

The observer gain l is chosen such that the eigenvalues of the error dynamics are at $820\,\mathrm{s^{-1}}$, $840\,\mathrm{s^{-1}}$, and $860\,\mathrm{s^{-1}}$. With this choice the cutoff frequency of transfer functions, $\omega \mapsto \mathcal{G}_y^{\hat{x}_k}(\mathrm{j}\omega), k \in \{1,2,3\}$, from the measurement y to the estimate $\hat{x}_k, k \in \{1,2,3\}$ of the observer (10) is also around $840\,\mathrm{rad/s}$. Furthermore, a notch filter, as described in Tietze et al. (2008, Sec. 13.8), is used to eliminate the dominant mechanical resonance frequency $942\,\mathrm{rad/s}$ of the plate corrupting the position measurement.

Comparing the amplitude spectrum of the transfer functions of the observer and the algebraic differentiators combined with the notch filter in Fig. 9, called $\bar{\mathcal{G}}_y^{\hat{x}_k}(\mathrm{j}\omega), k \in \{1,2,3\}$ and $\mathcal{D}_y^{\hat{y}^{(n)}}(\mathrm{j}\omega), n \in \{0,1,2\}$, respectively, shows similar results up to the cutoff frequency ω_c. For higher frequencies, according to Othmane et al. (2022, Sec. 4.2.2), the algebraic differentiators have a stopband slope of $20(\mu - n)\,\mathrm{dB}$ with $\mu = 1 + \min\{\alpha, \beta\}$ for the n-th order derivative, which would result, according to Fig. 9, in an unfair comparison of MBC and MFC. For this reason, additional low-pass filters are added to the estimations of the observer, to match the stopband slope of the algebraic differentiator. The resulting transfer functions of the observer, the low-pass, and the notch filter are denoted by $\tilde{\mathcal{G}}_y^{\hat{x}_k}(\mathrm{j}\omega), k \in \{1,2,3\}$.

A block diagram in Fig. 10 illustrates the estimation algorithms used. The observer (10), the notch filter, and the low-pass filters are discretised using Tustin's method with frequency prewarp of their respective cutoff frequency, resulting in a sharp drop of the transfer function near the Nyquist frequency $\omega_N = \frac{\pi}{t_s} \approx 1.0 \cdot 10^5\,\mathrm{Hz}$ in Fig. 9 (see also Oppenheim & Schafer, 1975, Sec. 5.1.3).

As mentioned before, the computational burden differs in the proposed algorithms. The MBC takes approximately 11.6% of the controller cycle, whereas the MFC law (14) with $N = 0$, $\alpha = \beta = 4$ and $\omega_c = 840\,\mathrm{rad/s}$ takes 49.7% of the cycle. The reason for this is the evaluation of several discrete convolutions, needed for the estimation. Nonetheless, a more efficient implementation of the MFC might be possible, but is out of the scope of this paper.

4.3. Trajectory tracking

In the following, the capabilities of the different algorithms designed in Section 3 are compared for different trajectory tracking scenarios.

4.3.1. Vertical motion

This experiment uses the same set point transition as described in Section 4.1 for the parametrisation of the algebraic differentiator. Fig. 11 shows the measured position y_1 in green and the reference trajectory $y_{r,1}$ in red when the MFC law (14) is used. Interestingly, the green graph is ahead of the reference, which will be clear by looking at the error $e_1(t) = y_1(t) - y_{r,1}(t)$. According to the discrete control law (25) the filtered measurement $\hat{y}_1(t)$ is used to calculate the error $\hat{e}_1(t) = \hat{y}_1(t) - y_{r,1}(t)$. The reason of being ahead of the reference is the known delay δ_t of the algebraic differentiator and the suggested choice to only filter the measured signals and not the errors as in Scherer et al. (2023). This results in a prediction of the reference signal and
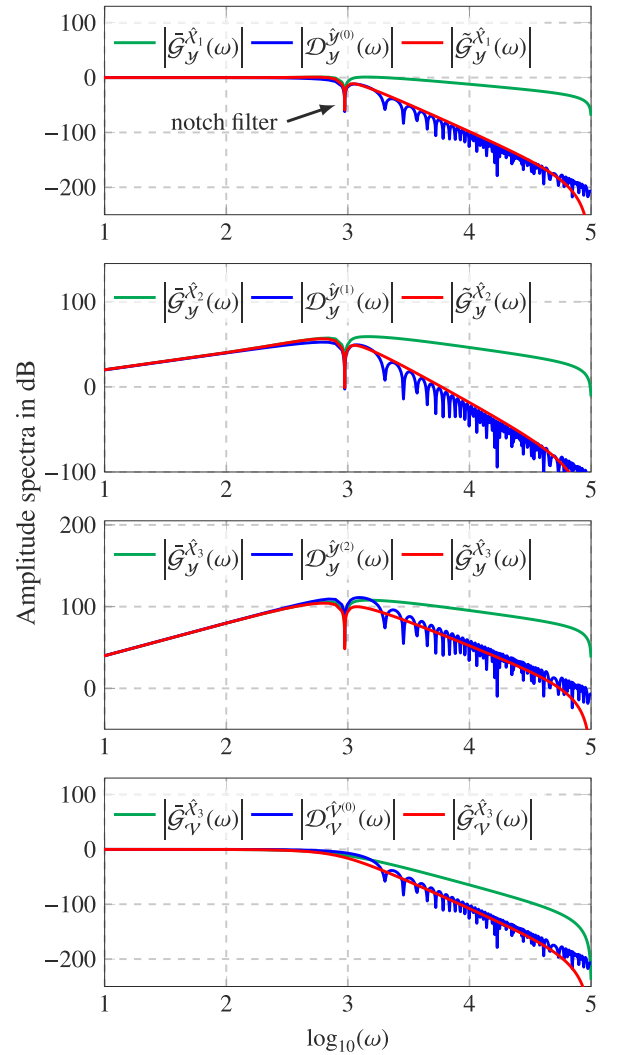

Fig. 9. Comparison of the amplitude spectra of the observer in combination with a notch filter $\omega \mapsto \left|\tilde{\mathcal{G}}_y^{\hat{x}_k}(\mathrm{j}\omega)\right|, k \in \{1,2,3\}$, the same combination extended with additional low-pass filters according to Fig. 10 $\omega \mapsto \left|\mathcal{D}_y^{\hat{y}^{(n)}}(\mathrm{j}\omega)\right|, n \in \{0,1,2\}$, and the algebraic differentiators with the notch filter $\omega \mapsto \left|\bar{\mathcal{G}}_y^{\hat{x}_k}(\mathrm{j}\omega)\right|, k \in \{1,2,3\}$.

the behaviour seen in Fig. 11, because the delay δ_t of the algebraic differentiator is known and independent of the filtered signal. This effect can be compensated by also delaying the reference signal, which results in the blue graph marked with $\bar{y}_1(t)$ matching the dashed reference. By also delaying the reference by δ_t, the error $\bar{e}_1(t) = \bar{y}_1(t) - y_{r,1}(t)$ shows the same course as $\hat{e}_1(t)$ up to more disturbances on $\bar{y}_1(t)$. The MBC is showing the same behaviour, because of the additional filters, but in this case the delay is unknown. Therefore, knowing exactly the signal independent delay of the algebraic differentiator is a significant advantage compared to a conventional low-pass filter.

In further experiments the RMS values of $\hat{e}_k, k \in \{1,2,3\}$, are used for a fair comparison of the algorithms, because $\hat{e}_k, k \in \{1,2,3\}$, are the errors the corresponding controller can react on. The values are summarised in Table 3 and marked with different colours. The MBC is seen as a benchmark, therefore, the values of this algorithm are given in black. If an algorithm can achieve a smaller RMS value, it is marked with green, otherwise with red. For the MBC and the MFC law (14) the experiment was repeated ten times, to calculate the mean value as well as the standard deviation of the RMS values. For both algorithms and all sensors, the standard deviation was smaller than
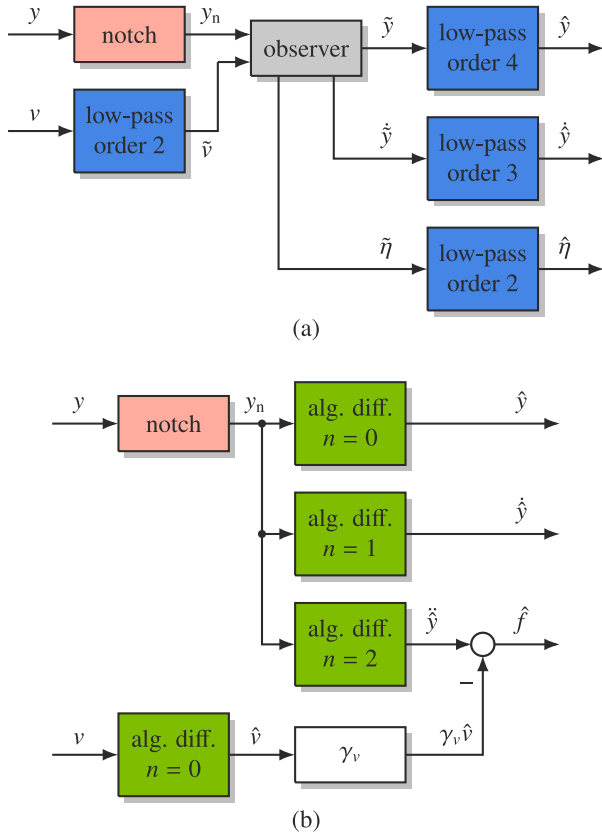
Fig. 10. Diagrams of the proposed estimation algorithms. (a) model based disturbance observer with additional low-pass and notch filters to ensure a fair comparison between the MBC and MFC, (b) estimation using algebraic differentiators and a notch filter for the proposed MFC.

Fig. 11. Results for the trajectory tracking of MFC law (14), to show the effect of the known delay δ_t introduced by the algebraic differentiator and how to compensate it.

30 nm, which is negligible in view of the resolution of the sensors. Therefore, only one experiment is performed and the resulting RMS values are compared. Table 3 reveals that the proposed MFC algorithms (14), (17), and (19) are outperforming the MBC. The RMS values of the errors obtained with the MFC control law (14) are approximately half as high as those observed with the MBC approach. It is also noticeable that in general using less model information results in higher RMS of the errors. Nonetheless, the control laws (17) and (19), with exception of the error in y_3, are still showing better results than the MBC. Only the MFC of the current (21) shows errors the RMS values of which are approximately five times higher than those with the other algorithms. This can be explained by the amount of model information used. Instead of the air gaps, the sensor values are used to calculate the input gains $\gamma_{i,k}, k \in \{1, 2, 3\}$. Moreover, a linear current model is assumed for the nonlinear behaviour of the magnets. Nevertheless, with this algorithm steady state accuracy is guaranteed.

4.3.2. Tilting of the plate

At the start of a tilting experiment, the plate hovers horizontally at a position of 2 mm. After that, three individual reference trajectories, with different transition times marked with dashed vertical lines, are planned as depicted in the first row of Fig. 12. The MBC and MFC law (14) use the pseudo inverse $B^\dagger$ to decouple the three points where the sensors are located. This model-based method is in contrast to the remaining MFC algorithms that have to realise the decoupling by the estimate of the disturbance f. The reason for this is that these algorithms are based on three ultra-local models that are only implicitly coupled by the disturbance f, as discussed in Section 3. Fig. 12 shows the results of tilting the plate using the MFC law (17). The second row
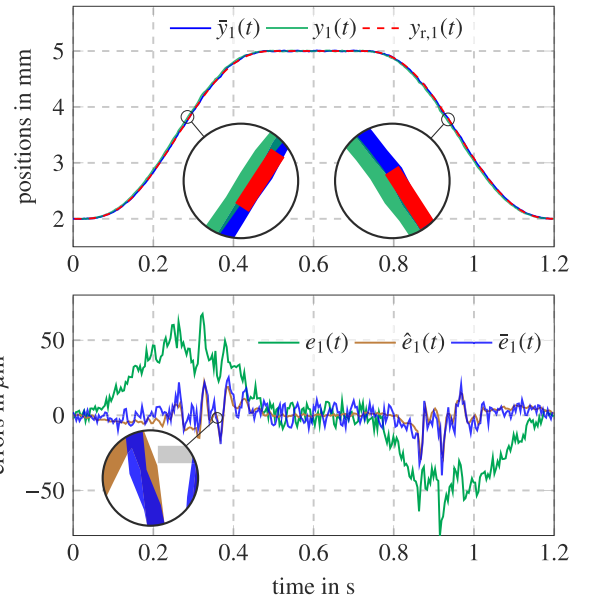
of this figure shows the errors $e_k(t), \hat{e}_k(t), k \in \{1, 2, 3\}$, and the third row the estimates $\hat{f}_{\bar{F},k}(t), k \in \{1, 2, 3\}$. Especially the plots of $\hat{e}_2(t)$ and $\hat{f}_{\bar{F},2}(t)$ are displaying the decoupling of the MFC. The transition of $y_2(t)$ is completed after 0.25 s, resulting in an error oscillating around zero and an estimation of the disturbance of approximately 13 m/s². Nonetheless, after 0.5 s the transition of $y_3(t)$ is completed as well and the estimate $\hat{f}_{\bar{F},2}(t)$ starts converging to 14 m/s², even though, the error $\hat{e}_2(t)$ still oscillates around zero. This example demonstrates that the MFC ensures the decoupling.

The RMS values in Table 3 show similar results as the vertical movement of the plate. The MFC law (14) is almost twice as accurate as the MBC and the algorithms (17) and (19) can obtain better results, except for $y_3(t)$. Again the MFC law (21) cannot achieve results that are as good as the other MFC laws. Nevertheless, the experiments show that a combination of the MFC with additional model information can lead to excellent results and outperform the MBC.

4.4. Robustness against sensor and actuator faults

The robustness with respect to actuator and sensors faults of the algorithms from Section 3 shall now be investigated. Therefore, the plate hovers horizontally at a position of 2 mm for each experiment.

4.4.1. Abrupt constant and multiplicative actuator fault

To investigate the robustness against abrupt actuator faults, these faults are modelled using the shifted Heaviside step function

$$\theta(t, \tau) = \begin{cases} 0, & t < \tau, \\ 1, & \tau \leq t. \end{cases} \quad (26)$$

For the abrupt fault at time τ the current $\Delta i_1(t, \tau) = K_i \theta(t, \tau)$ is added to $i_1(t)$, whereas $K_i = 400$ mA, which corresponds to 5% of the maximal current. To simulate a multiplicative fault, the current $i_1(t)$ is changed to $(1 + \bar{K}_i \theta(t, \tau))i_1(t)$, with $\bar{K}_i = 0.4$.

Fig. 13 shows the results of the abrupt constant actuator fault over time for the proposed algorithms. All have in common that after approximately 150 ms the measured values are back at the reference of 2 mm, which is the result of the same parametrisation of the controllers. The direct comparison in Table 3 shows that the quality gauge of the MFC law (14) is almost half as high compared to that of the
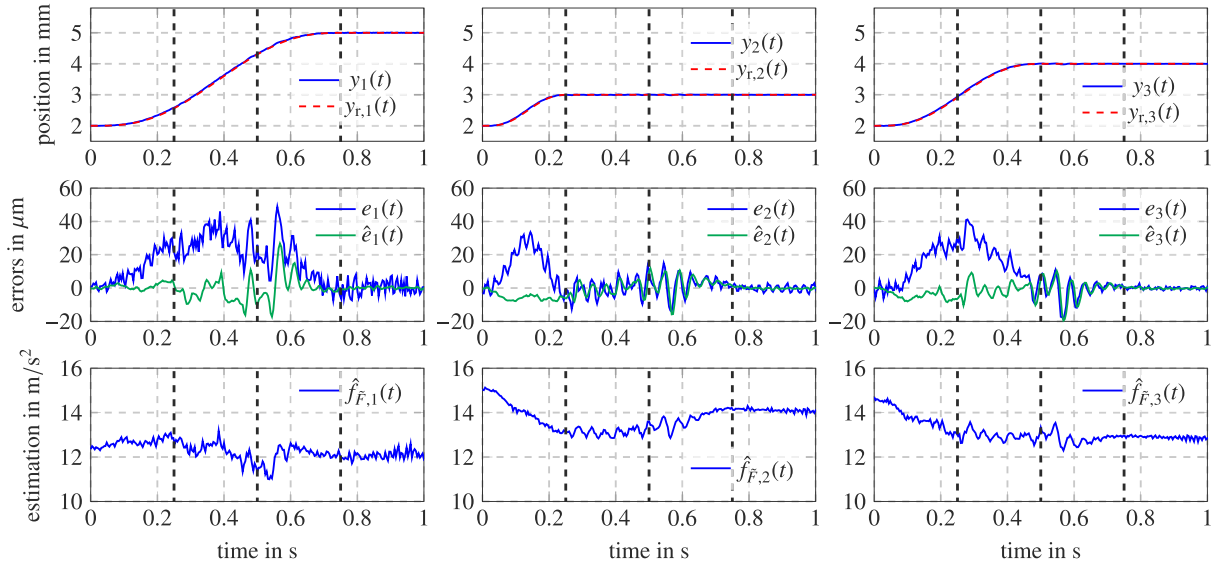
Fig. 12. Experimental results for the tilting of the plate with MFC law (17). The graphs show that the proposed MFC is capable of decoupling the three ultra-local models.

MBC. Additionally the minimal error of $\min(\hat{e}_1(t)) = -114.1$ μm is significantly smaller than the value of $\min(\hat{e}_1(t)) = -184.1$ μm for the MBC. This behaviour can be seen for all MFC algorithms, but for the remaining algorithms (17), (19) and (21) a decaying oscillation around the position 2 mm can be observed, which cannot be observed for the MBC and MFC law (14). Probably the reason for this is the choice of parameter $F_{d,4}$ and similarly for u and i, because the reaction to the disturbance resulting form the abrupt error is not distributed equally on all four magnets, as depicted in Fig. 14. The estimate of the disturbance for the MFC law (17) is shown with solid lines. For $\hat{f}_{\tilde{F},1}$ the reaction to the fault is immediate and can be compared to the reaction of the MBC depicted in the blue dashed line. The estimates $\hat{f}_{\tilde{F},2}$ and $\hat{f}_{\tilde{F},3}$ on the other hand are oscillating around $14.3\,\mathrm{m/s^2}$ and $15\,\mathrm{m/s^2}$, the values that they converge to, after the motion of the plate has stabilised after approximately 150 ms. The reaction of the MBC is different, because the control input v is split evenly to all magnets using the pseudo inverse $B^{\dagger}$. After the fault occurs, all estimates converge to lower values. This shows that in this case the implicit decoupling of the MFC algorithms (17), (19), and (21) is resulting in a different transient behaviour, whereas the MFC law (21) again provides results that are not as good compared to the other MFC algorithms.

According to Table 3, similar behaviour can be seen as for the abrupt actuator fault. Interestingly, the results from MFC law (17) show higher RMS values than the algorithm using the input u. This is because the plate started oscillating after the stabilisation. The reason for this behaviour is unknown.

4.4.2. Abrupt sensor fault

To simulate an abrupt sensor fault, the Heaviside step function (26) is used again. An error in the sensor value y_1 is modelled as $\Delta y_1(t, \tau) = K_y \theta(t, \tau)$ with $K_y = 0.2$ mm, which corresponds to 10% of the current sensor value. With this change, the sensor value becomes $y_1(t) + \Delta y_1(t, \tau)$. The results of this experiment in Table 3 show that the MFC cannot outperform the MBC. Comparing the estimate of the disturbance $\hat{f}_{v,1}(t)$ with $\hat{\eta}_1(t) + g$ in Fig. 15 shows that the peaks of $\hat{f}_{v,1}(t)$ are almost twice as high. This results from the additional low-pass filters depicted in Fig. 10, which will be clear by comparing the responses to a unit step in Fig. 15. There, the step responses of $-\omega^2 \mathcal{F}\{\ddot{g}\}(j\omega)$ and $\mathcal{G}_y^{\hat{x}_3}(j\omega)$ show almost the same maximum values, but adding the notch and low-pass filters changes the peaks of $\tilde{\mathcal{G}}_y^{\hat{x}_3}(j\omega)$ to approximately half of the values of $\mathcal{D}_y^{\hat{y}^{(2)}}(j\omega)$, which makes the MBC less sensitive to abrupt changes in the sensor value.
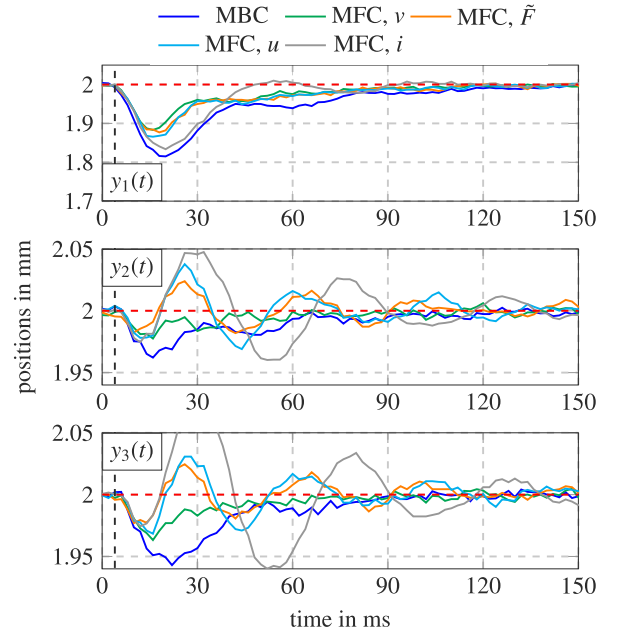

Fig. 13. Response of the different proposed controllers to an abrupt constant actuator fault. The MFC approaches show a high robustness against these faults.

5. Conclusion and future work

In this paper, a systematic tuning approach of a MFC algorithm for an unstable MIMO system that can be approximated by three implicitly coupled second-order differential equations is investigated. Numerous experiments carried out on a test bed show the capabilities of the MFC approaches combined with physically motivated model knowledge. The experiments show that the proposed algorithms can achieve a high level of robustness with respect to actuator faults and much better results if they are coupled with model information.

It could be seen that the MFC needs more computational power compared to the model based approach, because multiple convolutions have to be carried out. This has limited the choice of the cutoff frequency ω_c and the parameters $\alpha = \beta$ of the algebraic differentiators.

Table 3
Summary of the experimental results with the RMS values of $\hat{e}_k, k \in \{1,2,3\}$ as a quality gauge. The values of the MBC are seen as a benchmark and therefore depicted in black. If an algorithm can achieve lower RMS values it is marked in green, otherwise in red.

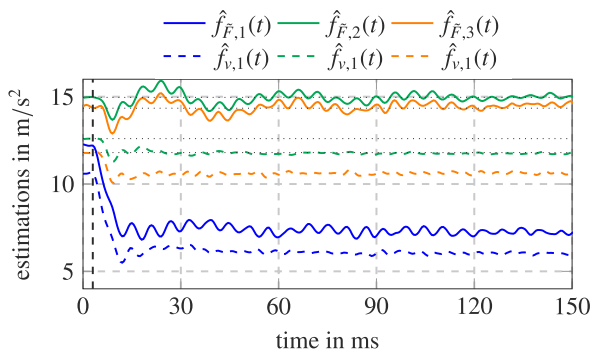| Experiment	Sensor	MBC	MFC, v	MFC, $\tilde{F}$	MFC, u	MFC, i
Horizontal movement	y_1	8.1 μm	5.1 μm	6.0 μm	6.6 μm	31.4 μm
	y_2	11.7 μm	6.2 μm	7.8 μm	8.6 μm	31.4 μm
	y_3	7.5 μm	4.2 μm	6.5 μm	8.8 μm	31.0 μm
Tilting the plate	y_1	6.2 μm	3.6 μm	4.6 μm	4.5 μm	24.6 μm
	y_2	4.7 μm	2.3 μm	3.8 μm	4.0 μm	15.9 μm
	y_3	3.4 μm	1.8 μm	3.8 μm	5.0 μm	19.9 μm
Abrupt actuator faults, i_1	y_1	37.2 μm	20.1 μm	22.3 μm	23.8 μm	29.9 μm
	y_2	6.5 μm	3.6 μm	5.0 μm	6.3 μm	10.9 μm
	y_3	10.7 μm	5.6 μm	5.3 μm	6.7 μm	16.8 μm
Multiplicative actuator fault, i_1	y_1	46.4 μm	27.2 μm	42.8 μm	29.4 μm	35.3 μm
	y_2	8.6 μm	4.9 μm	7.7 μm	6.3 μm	12.0 μm
	y_3	13.5 μm	7.2 μm	11.3 μm	6.9 μm	18.6 μm
Abrupt Sensor fault, y_1	y_1	41.9 μm	56.4 μm	45.8 μm	17.0 μm	46.1 μm
	y_2	10.6 μm	8.8 μm	21.0 μm	14.6 μm	28.6 μm
	y_3	10.4 μm	5.7 μm	24.9 μm	19.2 μm	50.3 μm

Fig. 14. Estimation of the disturbance of MFC laws (14) and (17) caused by an abrupt constant actuator fault. The plot illustrates the different decoupling strategies used, on the one hand the pseudo inverse $B^\dagger$ and on the other hand $F_{d,4} = \frac{1}{2}(\tilde{F}_2 + \tilde{F}_3)$.
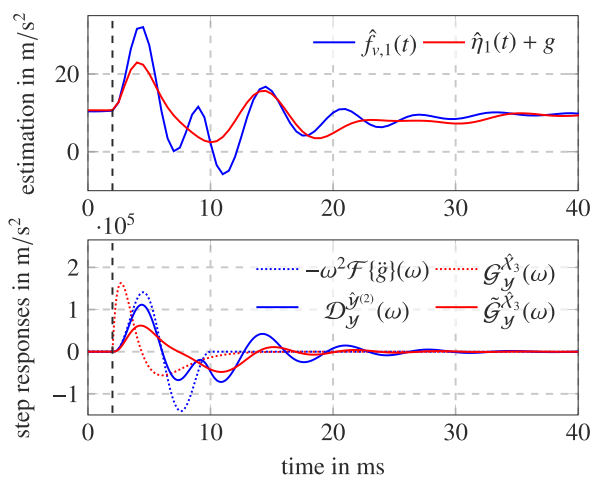

Fig. 15. Estimation of the disturbance of MBC and MFC law (14) for an abrupt sensor fault and the responses of several filters to a unit step starting at $t = 2\,\text{ms}$. The reaction of the MBC is less dominant compared to the MFC.

As stated before, a more efficient implementation of the convolution integrals of the MFC is possible, e.g. by using dedicated signal processors. However, this is out of the scope of the present paper. Nonetheless, using the differentiators has shown to be beneficial, because this signal based approach does not rely on a model of the system to estimate unknown quantities, compared to a classical observer based approach. However, this comes with the price that results of the estimates of the disturbance f are harder to interpret, if no mathematical model of the system is available. To realise a fair comparison of the proposed MBC and the MFC law (14), additional low-pass filters are added to the disturbance observer, to match the filter order of the used algebraic differentiators.

Future work should investigate why some parameter combinations of the algebraic differentiator are resulting in an unstable closed-loop system, or respectively what the parameter combinations resulting in a stable closed loop have in common. Further, the estimation delay should explicitly be taken into account during the controller design. Additionally, a systematic tuning approach without parameter sweeps that are carried out on the test bed would be beneficial. Similarly, approximations with higher order systems are still open for investigation. This also goes along with the estimation of higher order derivatives, which probably needs more computation time, a problem that has to be tackled as must be the discretisation of the algebraic differentiators.

CRediT authorship contribution statement

P.M. Scherer: Writing – review & editing, Writing – original draft, Visualization, Software, Methodology, Investigation, Data curation. **A. Othmane:** Writing – review & editing, Formal analysis, Conceptualization. **J. Rudolph:** Writing – review & editing.

Declaration of competing interest

The authors declare that they have no known competing financial interests or personal relationships that could have appeared to influence the work reported in this paper.

Acknowledgement

Appendix A. Information about algebraic differentiators

In this section, useful background information on algebraic differentiators, initially developed in Mboup et al. (2007, 2009) are recalled. The interested reader is referred to Othmane et al. (2022) for an overview on this topic and Szegö (1939) for the discussion and analyses of the required orthogonal polynomials.

In the sequel Γ denotes the gamma function and

$$w^{(\alpha,\beta)}(\tau) = \begin{cases} (1-\tau)^\alpha(1+\tau)^\beta, & \tau \in [-1,1], \\ 0, & \text{otherwise,} \end{cases}$$

with real scalar parameters $\alpha, \beta > -1$, is the weight function associated with the orthogonal Jacobi polynomial of degree $N \in \mathbb{N}$ defined as

$$P_N^{(\alpha,\beta)}(\tau) = \sum_{k=0}^N \binom{N}{k} c_k^{(\alpha,\beta)}(\tau-1)^k,$$

$$c_k^{(\alpha,\beta)} = \frac{\Gamma(\alpha+N+1)\Gamma(\alpha+\beta+N+k+1)}{2^k N! \Gamma(\alpha+\beta+N+1)\Gamma(\alpha+k+1)}.$$

Denote by $x^{(n)}$ the n-th order derivative of a function x, where $x^{(0)}$ denotes the function x itself. Assume for an arbitrary n that $x^{(n)}$ is square Lebesgue integrable and let $\alpha, \beta \in \mathbb{R}$ be arbitrary such that $\min(\alpha, \beta) > n - 1$. Then, $x^{(n)}$ can be approximated by a N-th order truncated generalised Fourier expansion as

$$\hat{x}^{(n)}(t) = \int_{t-T}^t g^{(n)}(t-\tau)x(\tau)d\tau, \quad g(\tau) = g_{N,T,\vartheta}^{(\alpha,\beta)}(\tau) \tag{A.1}$$

with the kernel

$$g(\tau) = \begin{cases} \frac{2w^{(\alpha,\beta)}(\nu(\tau))}{T} \sum_{j=0}^N \frac{P_j^{(\alpha,\beta)}(\vartheta)}{\left\|P_j^{(\alpha,\beta)}\right\|^2} P_j^{(\alpha,\beta)}(\nu(\tau)), & \tau \in [0,T], \\ 0, & \text{otherwise,} \end{cases}$$

depending on ϑ parametrising the approximation delay and $\nu(\tau) = 1 - 2\tau/T$, where $\|z\| = \sqrt{\langle z, z \rangle}$ is the norm induced by the inner product

$$\langle z, y \rangle = \int_{-1}^1 w^{(\alpha,\beta)}(\tau)z(\tau)y(\tau)d\tau.$$

All calculations are based on the sliding time window $[t-T, t]$, where T describes the filter window length, associated with the cutoff frequency ω_c, as discussed in Kiltz and Rudolph (2013). As first pointed out in Mboup et al. (2009), the estimate is delayed by a small but known delay given as

$$\delta_t = \begin{cases} \frac{\alpha+1}{\alpha+\beta+2}T, & N = 0, \\ \frac{1-\vartheta}{2}T, & N \neq 0. \end{cases}$$

A delay-free estimation is possible by choosing $N > 0$ and $\vartheta = 1$. However, accepting a delay increases the accuracy of the approximation and yields desirable frequency-domain properties (see Mboup et al., 2009; Mboup & Riachy, 2014, 2018 and Othmane et al., 2022).

The estimate of $\hat{x}^{(n)}$ can be interpreted as the output of a finite impulse response (FIR) filter driven by the input x. The kernel $g_{N,T,\vartheta}^{(\alpha,\beta)}$ has also a system theoretic interpretation. As shown for example in Kiltz (2017) or Othmane et al. (2022) and used in Section 4.1, $g_{N,T,\vartheta}^{(\alpha,\beta)}$ can be interpreted as a low-pass filter driven by the sought derivative $x^{(n)}$ and with cutoff frequency ω_c. This interpretation makes the filter design more intuitive.

All considerations so far were done in a continuous time setting. Nonetheless, for the implementation of the algorithms suggested in this contribution, a discrete-time realisation of the estimators is required. Therefore, the integral (A.1) has to be discretised using an appropriate quadrature method. For that, equidistant sampling with t_s is considered. This results in a filter window of length T that is of an integral multiple of the sampling time t_s, i.e. $T = n_s t_s$. The abbreviation $x[k] = x(kt_s), k \in \mathbb{N}$ is used for x evaluated at the time kt_s. With this notation, the convolution (A.1) can be approximated with

$$\hat{x}^{(n)}[k+\theta] = \frac{1}{\Phi}\sum_{j=0}^{L-1} w_n[j]x[k-j], \quad \Phi = \frac{t_s^n}{n!}\sum_{j=0}^{L-1} w_n[j](-j)^n,$$

where the parameters θ, L, and $w_n[j]$ depend on the numerical integration method used, as described in Othmane, Mounier, and Rudolph (2021). For instance, for the mid-point rule $\theta = 1/2$, $L = n_s$, and $w_n[j] = t_s g^{(n)}[j + 1/2]$. The design and discretisation of the differentiators are done using the open-source toolbox AlgDiff (see Othmane, 2022), which comes with detailed examples for a correct application of the filters.

Appendix B. Derivation of the MFC

In the following, the MFC for a second order ultra-local model is derived using the Laplace transformation and it is shown that it is a special case of the considerations made in Section 3.3.

B.1. An algebraic point of view

Consider the second order ultra-local model

$$\ddot{y}(t) = \gamma u(t) + f(t), \tag{B.1}$$

with measurement $y(t)$, input $u(t)$, input gain $\gamma \in \mathbb{R}$ and piecewise constant disturbance $f(t)$. Applying the Laplace transform to (B.1) under the assumption that $f(t)$ is constant on the interval $[0, T]$ yields

$$s^2 Y(s) - \dot{y}(0) - s y(0) = \gamma U(s) + \frac{1}{s}F \tag{B.2}$$

with $Y(s)$, $U(s)$ and F the Laplace transform of $y(t)$, $u(t)$ and $f(t)$, respectively, and the initial conditions $y(0)$ and $\dot{y}(0)$. To get rid of the initial conditions, (B.2) is differentiated twice with respect to s yielding

$$2Y(s) + 4s\frac{dY}{ds}(s) + s^2\frac{d^2Y}{ds^2}(s) = \gamma\frac{d^2U}{ds^2}(s) + \frac{2}{s^3}F. \tag{B.3}$$

In the latter equation the expressions $s^2\frac{d^2Y}{ds^2}(s)$ and $4s\frac{dY}{ds}(s)$ are hindering an implementation. Therefore, (B.3) is multiplied by s^{-2} and again by s^{-1} to remove differentiation in the time domain and increase the noise attenuation, respectively, which results in

$$\frac{2}{s^3}Y(s) + \frac{4}{s^2}\frac{dY}{ds}(s) + \frac{1}{s}\frac{d^2Y}{ds^2}(s) = \gamma\frac{1}{s^3}\frac{d^2U}{ds^2}(s) + \frac{2}{s^6}F. \tag{B.4}$$

With this, only integrals of measured signals occur when the expressions are transformed back into the time domain, which will be the next step. Therefore, the following inverse transformations

$$\frac{d^n}{ds^n}X(s) \bullet\!\!-\!\!\circ (-t)^n x(t) \tag{B.5a}$$

$$\frac{1}{s^n} \bullet\!\!-\!\!\circ \frac{t^{n-1}}{(n-1)!} \tag{B.5b}$$

$$\frac{X(s)}{s} \bullet\!\!-\!\!\circ \int_0^t x(\sigma)d\sigma. \tag{B.5c}$$

are used (see e.g. in the appendix of Doetsch, 1974). Applying them to (B.4) and rearranging the expressions yields

$$\frac{2t^5}{5!}\hat{f} = 2\int_0^t\int_0^{\sigma_1}\int_0^{\sigma_2} y(\tau)d\tau d\sigma_1 d\sigma_2$$

$$- 4\int_0^t\int_0^{\sigma_1}\tau y(\tau)d\tau d\sigma_1 + \int_0^t \tau^2 y(\tau)d\tau$$

$$- \gamma\int_0^t\int_0^{\sigma_1}\int_0^{\sigma_2}\tau^2 u(\tau)d\tau d\sigma_1 d\sigma_2.$$

Now the Cauchy-formula for repeated integration (see e.g. Chapter 11 in Doetsch (1974)) can be used to simplify the expression for $\hat{f}$, resulting in

$$\hat{f} = \frac{5!}{2t^5} \int_0^t \left[(t-\tau)^2 - 4(t-\tau)\tau + \tau^2 \right] y(\tau) - \frac{\gamma}{2}(t-\tau)^2 \tau^2 u(\tau) \mathrm{d}\tau.$$

Considering only the interval $[0, T]$ instead of $[0, t]$ and further simplifying the equation yields

$$\hat{f} = \frac{5!}{2T^5} \int_0^T \left(T^2 - 6T\tau + 6\tau^2 \right) y(\tau) - \frac{\gamma}{2}(T-\tau)^2 \tau^2 u(\tau) \mathrm{d}\tau.$$

A moving time window $[t - T - \varepsilon, t - \varepsilon], \varepsilon > 0$ can be introduced by evaluating the signals y and u at $\sigma + t - T - \varepsilon$ instead of σ. With this change, the expression

$$\hat{f}(t) = \frac{5!}{2T^5} \int_0^T \left(T^2 - 6T\sigma + 6\sigma^2 \right) y(\sigma + t - T - \varepsilon) \\ - \frac{\gamma}{2}(T - \sigma)^2 \sigma^2 u(\sigma + t - T - \varepsilon) \mathrm{d}\sigma$$

is now a function of time. Thereafter, the substitution $\tau = \sigma + t - T - \varepsilon$ leads to

$$\hat{f}(t) = \frac{5!}{2T^5} \int_{t-T-\varepsilon}^{t-\varepsilon} \left(T^2 - 6T(t-\tau-\varepsilon) + 6(t-\tau-\varepsilon)^2 \right) y(\tau) \\ - \frac{\gamma}{2}(t-\tau-\varepsilon)^2 (T-(t-\tau-\varepsilon))^2 u(\tau) \mathrm{d}\tau. \tag{B.6}$$

This expression for the estimation of f is slightly different from that commonly used in the literature (e.g. Bekcheva et al., 2018 or Barth et al., 2020) in the sense that the current time t appears in the filter kernel and the parameter ε is explicitly considered.

B.2. A system theoretic point of view

The estimation of $f(t)$ according to the ultra-local model (B.1) reads

$$\hat{f}(t) = \int_{t-T-\varepsilon}^{t-\varepsilon} g(t-\tau-\varepsilon) f(\tau) \mathrm{d}\tau, \quad \varepsilon > 0, \tag{B.7a}$$

$$= \int_{t-T-\varepsilon}^{t-\varepsilon} \ddot{g}(t-\tau-\varepsilon) y(\tau) - \gamma g(t-\tau-\varepsilon) u(\tau) \mathrm{d}\tau \tag{B.7b}$$

with $g = g_{N,T,\vartheta}^{(\alpha,\beta)}$ denoting the kernel of the algebraic differentiator presented in Appendix A. Now consider the special parametrisation $N = 0$, which leads to the kernel

$$g_{0,T,\vartheta}^{(\alpha,\beta)}(\tau) = \begin{cases} \frac{(\alpha+\beta+1)!}{\alpha! \beta! T^{\alpha+\beta+1}} \tau^\alpha (T-\tau)^\beta, & \tau \in [0, T], \\ 0, & \text{otherwise.} \end{cases} \tag{B.8}$$

If the parameters $\alpha = \beta = 2$ are chosen, the kernel (B.8) further simplifies to

$$g_{0,T,\vartheta}^{(2,2)}(\tau) = \bar{g}(\tau) = \begin{cases} \frac{1}{2} \frac{5!}{2T^5} \tau^2 (T-\tau)^2, & \tau \in [0, T], \\ 0, & \text{otherwise.} \end{cases} \tag{B.9}$$

Calculating the second derivative of $\bar{g}$ with respect to τ leads to

$$\frac{\mathrm{d}^2 \bar{g}}{\mathrm{d}\tau^2}(\tau) = \begin{cases} \frac{5!}{2T^5}(6\tau^2 - 6T\tau + T^2), & \tau \in [0, T], \\ 0, & \text{otherwise.} \end{cases} \tag{B.10}$$

Using both (B.9) and (B.10) in (B.7) results in an expression that is equivalent to (B.6). This shows, that the propositions made in this paper are a generalisation of the ansatz that is commonly used in the literature. As seen in Section 4 this generalisation is needed in some cases to realise the MFC.

B.3. Validation of the derivation

To validate the calculations made in this section, consider the differential equation

$$\ddot{y}(t) = F, \tag{B.11}$$

with $F \in \mathbb{R}$, the solution of which is $y(t) = \frac{1}{2} F t^2$. The relation (B.6) with $u(t) = 0$ can now be used together with the solution of the differential equation (B.11) to estimate the parameter F resulting in

$$\hat{F}(t) = \int_{t-T-\varepsilon}^{t-\varepsilon} \ddot{\bar{g}}(t-\tau) y(\tau) \mathrm{d}\tau$$

$$= \frac{5!}{2T^5} \int_{t-T-\varepsilon}^{t-\varepsilon} \left(T^2 - 6T(t-\tau-\varepsilon) + 6(t-\tau-\varepsilon)^2 \right) \frac{1}{2} F \tau^2 \mathrm{d}\tau$$

$$= F.$$

The reason for this result lies in the approximation of the second order derivative of $y(t)$ with a constant according to the choice of $N = 0$. For further theoretical analysis the degree of exactness introduced in Kiltz (2017) can be considered (see also Othmane et al., 2022). The results $\hat{F} = F$ shows that the calculations made in this section are correct.

References

Al Younes, Y., Drak, A., Noura, H., Rabhi, A., & El Hajjaji, A. (2014). Model-Free Control of a Quadrotor Vehicle. In *2014 International Conference on Unmanned Aircraft Systems* (pp. 1126–1131). IEEE.

Barth, J., Condomines, J. P., Bronz, M., Moschetta, J. M., Join, C., & Fliess, M. (2020). Model-free control algorithms for micro air vehicles with transitioning flight capabilities. *International Journal of Micro Air Vehicles, 12*, 1–22.

Bekcheva, M., Join, C., & Mounier, H. (2018). Cascaded Model-Free Control for trajectory tracking of quadrotors. In *2018 International Conference on Unmanned Aircraft Systems* (pp. 1359–1368). IEEE.

Belhadjoudja, M. C., Maghenem, M., & Witrant, E. (2023). On the Intelligent Proportional Controller Applied to Linear Systems. In *62nd IEEE Conference on Decision and Control* (pp. 938–943). IEEE.

Carvalho, A. D., Pereira, B. S., Angélico, B. A., Laganá, A. A. M., & Justo, J. F. (2024). Model-free control applied to a direct injection system: Experimental validation. *Fuel, 358*, Article 130071.

Collon, C., Eckhardt, S., & Rudolph, J. (2007). A network approach to the modelling of active magnetic bearings. *Mathematical and Computer Modelling of Dynamical Systems, 13*(5), 455–469.

De Miras, J., Join, C., Fliess, M., Riachy, S., & Bonnet, S. (2013). Active magnetic bearing: A new step for model-free control. In *52nd IEEE Conference on Decision and Control* (pp. 7449–7454). IEEE.

Doetsch, G. (1974). *Introduction to the Theory and Application of the Laplace Transformation*. Springer.

Eckhardt, S., & Rudolph, J. (2004). High precision synchronous tool path tracking with an AMB machine tool spindle. In *9th International Symposium on Magnetic Bearings*.

Ellis, R. W., & Mote, C. D. (1977). A feedback vibration controller for circular saws. In *Joint Automatic Control Conference, No. 14* (pp. 1193–1198).

Fliess, M., & Join, C. (2008). Commande sans modèle et commande à modèle restreint. *e-STA Sciences et Technologies de l'Automatique, 5*(4), 1–23.

Fliess, M., & Join, C. (2009). Model-free control and intelligent PID controllers: Towards a possible trivialization of nonlinear control? *IFAC Proceedings Volumes, 42*(10), 1531–1550.

Fliess, M., & Join, C. (2013). Model-free control. *International Journal of Control, 86*(12), 2228–2252.

Fliess, M., & Join, C. (2023). Towards a control-theoretic trivialization of ABR video streaming. http://dx.doi.org/10.48550/arXiv.2310.00934, arXiv preprint arXiv: 2310.00934.

Haddar, M., Chaari, R., Baslamisli, S. C., Chaari, F., & Haddar, M. (2019). Intelligent PD controller design for active suspension system based on robust model-free control strategy. *Proceedings of the Institution of Mechanical Engineers, Part C, 233*(14), 4863–4880.

Hegedűs, T., Fényes, D., Németh, B., Szabó, Z., & Gáspár, P. (2022). Design of Model Free Control with tuning method on ultra-local model for lateral vehicle control purposes. In *2022 American Control Conference* (pp. 4101–4106).

Kiltz, L. (2017). *Algebraische Ableitungsschätzer in Theorie und Anwendung* (Ph.D. thesis), Saarland University, Germany.

Kiltz, L., Join, C., Mboup, M., & Rudolph, J. (2014). Fault-tolerant control based on algebraic derivative estimation applied on a magnetically supported plate. *Control Engineering Practice, 26*, 107–115.

Kiltz, L., Mboup, M., & Rudolph, J. (2012). Fault diagnosis on a magnetically supported plate. In *2012 1st International Conference on Systems and Computer Science* (pp. 1–6). IEEE.

Kiltz, L., & Rudolph, J. (2013). Parametrization of algebraic numerical differentiators to achieve desired filter characteristics. In *52nd IEEE Conference on Decision and Control* (pp. 7010–7015).

Lafont, F., Balmat, J.-F., Join, C., & Fliess, M. (2020). First steps toward a simple but efficient model-free control synthesis for variable-speed wind turbines. http://dx.doi.org/10.46300/9106.2020.14.146, arXiv preprint arXiv:2011.06415.

Lafont, F., Balmat, J.-F., Pessel, N., & Fliess, M. (2015). A model-free control strategy for an experimental greenhouse with an application to fault accommodation. *Computers and Electronics in Agriculture, 110*, 139–149.

Lei, S., & Palazzolo, A. (2008). Control of flexible rotor systems with active magnetic bearings. *Journal of Sound and Vibration, 314*(1–2), 19–38.

Li, W., Yuan, H., Li, S., & Zhu, J. (2022). A Revisit to Model-Free Control. *IEEE Transactions on Power Electronics, 37*(12), 14408–14421.

Mboup, M., Join, C., & Fliess, M. (2007). A revised look at numerical differentiation with an application to nonlinear feedback control. In *Proceedings of the 15th Mediterranean Conference on Control and Automation*.

Mboup, M., Join, C., & Fliess, M. (2009). Numerical differentiation with annihilators in noisy environment. *Numerical Algorithms*, *50*(4), 439–467.

Mboup, M., & Riachy, S. (2014). A Frequency Domain Interpretation of the Algebraic Differentiators. *IFAC Proceedings Volumes*, *47*(3), 9147–9151.

Mboup, M., & Riachy, S. (2018). Frequency-domain analysis and tuning of the algebraic differentiators. *International Journal of Control*, *91*(9), 2073–2081.

Moraes, M. S., & da Silva, P. S. P. (2015). Model-free control of magnetic levitation systems through algebraic derivative estimation. In *Proceedings 23rd ABCM International Congress of Mechanical Engineering*.

Neves, G. P., & Angélico, B. A. (2021). Model-free control of mechatronic systems based on algebraic estimation. *Asian Journal of Control*, *24*(4), 1575–1584.

Oppenheim, A. V., & Schafer, R. W. (1975). *Digital Signal Processing*. Englewood Cliffs, N. J.: Prentice-Hall Inc.

Othmane, A. (2022). AlgDiff: A Python package with MATLAB coupling implementing all necessary tools for the design, analysis, and discretization of algebraic differentiators. http://dx.doi.org/10.5281/zenodo.5172198, Available at https://github.com/aothmane-control/Algebraic-differentiators, version 2.3.

Othmane, A., Kiltz, L., & Rudolph, J. (2022). Survey on algebraic numerical differentiation: Historical developments, parametrization, examples, and applications. *International Journal of Systems Science*, *53*(9), 1848–1887.

Othmane, A., Mounier, H., & Rudolph, J. (2021). Parametrization of algebraic differentiators for disturbance annihilation with an application to the differentiation of quantized signals. *IFAC-PapersOnLine*, *54*(9), 335–340.

Othmane, A., & Rudolph, J. (2023). AlgDiff: An open source toolbox for the design, analysis and discretisation of algebraic differentiators. *at-Automatisierungstechnik*, *71*(8), 612–623.

Othmane, A., Rudolph, J., & Mounier, H. (2021). Systematic comparison of numerical differentiators and an application to model-free control. *European Journal of Control*, *62*, 113–119.

Rudolph, J. (2021). *Flatness-based control: An Introduction*. Shaker Verlag.

Scherer, P. M., Othmane, A., & Rudolph, J. (2023). Combining model-based and model-free approaches for the control of an electro-hydraulic system. *Control Engineering Practice*, *133*, Article 105453.

Szegö, G. (1939). *Orthogonal Polynomials*. New York: AMS.

Tabuada, P., Ma, W.-L., Grizzle, J., & Ames, A. D. (2017). Data-driven control for feedback linearizable single-input systems. In *56th IEEE Conference on Decision and Control* (pp. 6265–6270). IEEE.

Tietze, U., Schenk, C., & Gamm, E. (2008). *Electronic Circuits*. Berlin, Heidelberg: Springer.

Villagra, J., & Herrero-Pérez, D. (2012). A comparison of control techniques for robust docking maneuvers of an AGV. *IEEE Transactions on Control Systems Technology*, *20*(4), 1116–1123.

Wachter, J., Gröll, L., & Hagenmeyer, V. (2023). Application of Model-Free Control to Reduce the Total Harmonic Distortion of Inverters. In *2023 8th IEEE Workshop on the Electronic Grid* (pp. 1–7).

Zhang, H., Li, H., Mao, J., Pan, C., & Luan, Z. (2022). Model-free control of single-phase boost AC/DC converters. *IEEE Transactions on Power Electronics*, *37*(10), 11828–11838.